

Plasma-enhanced atomic layer deposition: Correlating O₂ plasma parameters and species to blister formation and conformal film growth

Cite as: J. Vac. Sci. Technol. A **39**, 062402 (2021); <https://doi.org/10.1116/6.0001094>

Submitted: 22 April 2021 • Accepted: 26 August 2021 • Published Online: 14 September 2021

 Andreas Werbrouck,  Kevin Van de Kerckhove,  Diederik Depla, et al.

COLLECTIONS

Paper published as part of the special topic on [Atomic Layer Deposition \(ALD\)](#)



View Online



Export Citation



CrossMark

ARTICLES YOU MAY BE INTERESTED IN

[Innovative remote plasma source for atomic layer deposition for GaN devices](#)

Journal of Vacuum Science & Technology A **39**, 062403 (2021); <https://doi.org/10.1116/6.0001318>

[Status and prospects of plasma-assisted atomic layer deposition](#)

Journal of Vacuum Science & Technology A **37**, 030902 (2019); <https://doi.org/10.1116/1.5088582>

[Conformality in atomic layer deposition: Current status overview of analysis and modelling](#)

Applied Physics Reviews **6**, 021302 (2019); <https://doi.org/10.1063/1.5060967>





Instruments for Advanced Science

- Knowledge,
- Experience,
- Expertise

Click to view our product catalogue

Contact Hiden Analytical for further details:
www.HidenAnalytical.com
info@hideninc.com



Gas Analysis

- ▶ dynamic measurement of reaction gas streams
- ▶ catalysis and thermal analysis
- ▶ molecular beam studies
- ▶ dissolved species probes
- ▶ fermentation, environmental and ecological studies



Surface Science

- ▶ UHVTPD
- ▶ SIMS
- ▶ end point detection in ion beam etch
- ▶ elemental imaging - surface mapping



Plasma Diagnostics

- ▶ plasma source characterization
- ▶ etch and deposition process reaction kinetic studies
- ▶ analysis of neutral and radical species



Vacuum Analysis

- ▶ partial pressure measurement and control of process gases
- ▶ reactive sputter process control
- ▶ vacuum diagnostics
- ▶ vacuum coating process monitoring

Plasma-enhanced atomic layer deposition: Correlating O₂ plasma parameters and species to blister formation and conformal film growth

Cite as: J. Vac. Sci. Technol. A 39, 062402 (2021); doi: 10.1116/6.0001094

Submitted: 22 April 2021 · Accepted: 26 August 2021 ·

Published Online: 14 September 2021



Andreas Werbrouck,  Kevin Van de Kerckhove,  Diederik Depla,  Dirk Poelman,  Philippe F. Smet, 
Jolien Dendooven,  and Christophe Detavernier^{a)} 

AFFILIATIONS

Department of Solid State Sciences, Ghent University, Krijgslaan 281-S1, Ghent 9000, Belgium

Note: This paper is part of the 2022 Special Topic Collection on Atomic Layer Deposition (ALD).

^{a)} **Author to whom correspondence should be addressed:** Christophe.Detavernier@ugent.be

ABSTRACT

Plasma-enhanced atomic layer deposition has gained a lot of attraction over the past few years. A myriad of processes have been reported, several reviews have been written on this topic, and there is a lot of interest for industrial applications. Still, when developing new processes, often heuristic approaches are used, choosing plasma parameters that worked for earlier processes. This can result in suboptimal plasma process conditions. In order to rationally decide which parameters to use, we systematically studied an inductively coupled RF oxygen plasma source (13.56 MHz) for powers up to 300 W, a pressure range between 10⁻⁴ and 10⁻² mbar, and a flow range between 10 and 400 sccm. We discerned between chemically active “radical” species (atomic O and excited, metastable O₂) and ionic particles (O₂⁺, O⁺, O₂⁻, and O⁻), which can have an additional physical effect to the film. Optical emission spectroscopy (OES) was used to study the generation of O₂⁺ and atomic O in the plasma source region. It is shown that the concentration of plasma species increases in a linear way with the plasma power and that the atom-to-ion fraction increases with both the power and the gas flow. To study the effect of plasma species in the remote region, near the sample position, an electrostatic quadrupole analyzer was used to gauge fluxes of O₂⁺, O⁺, O₂⁻, and O⁻. Even a moderate increase in pressure can drastically reduce the ion flux toward the substrate. The formation of bubbles or blisters in films can be linked to ion-induced compressive stress, and, hence, it can be mitigated by an increase in the gas pressure. Finally, Al₂O₃ was deposited in lateral high-aspect ratio structures to investigate the effect of plasma power and gas pressure on the partial pressure of radical species. Simulated profiles were fitted to experimental deposition profiles to estimate trends in the radical partial pressure, and a linear relationship between radical partial pressure and the power was found. This correlated with the density of atomic O species as observed in the OES measurements in the plasma source region. The methods presented in this work are also applicable to characterize other reactor geometries, plasma sources, and gas mixtures.

Published under an exclusive license by the AVS. <https://doi.org/10.1116/6.0001094>

I. INTRODUCTION

Atomic layer deposition (ALD) is a coating technique that is capable of coating complex and challenging substrates in a uniform and conformal way with the Å-level thickness control. It achieves this by the sequential pulsing of precursor molecules in the gas phase and reactant gases (e.g., H₂O, O₂, O₃, N₂, H₂, NH₃, and H₂S), which are either temporally or spatially separated, typically in an AB-type cycle¹ (with A and B denoting the different pulses). In this way, the reagents can only react on the available surface. Because the reactions are self-limiting, the amount of material

deposited per pulse (or per AB-cycle) is precisely controlled. To avoid precursor condensation and to assist in overcoming the reaction barrier of the chemical process, the substrate very often needs to be maintained at an elevated temperature. On the other hand, this temperature should not be too high to avoid decomposition of the precursor molecule (typically below ~300 °C, although this is very precursor-dependent). Numerous ALD processes have been developed in this way. Sometimes process development is hampered by lack of reactivity and other factors, resulting in no, or extremely slow, growth. Additionally, at lower temperatures, more

impurities from the precursors may be incorporated into the film. To alleviate these issues, one of the steps in the AB-sequence can be altered by means of a plasma. This way, new, activated species are created, opening up reaction pathways that are not available for thermal ALD processes. This extension of thermal ALD is called plasma-enhanced atomic layer deposition (PEALD).²

A. Challenges for PEALD

Recently, Knoops *et al.*² had reviewed applications, materials, reactor designs, and challenges for PEALD. PEALD-deposited thin films have fewer impurities and are denser than thermally grown ALD films. Lower substrate temperatures become accessible, while the precise thickness control and uniformity of thermal ALD are maintained. On the other hand, the highly energetic species and UV radiation from the plasma can damage the films, conformality is harder to achieve than with thermal ALD, and often process parameters are chosen in a heuristic way.

1. Ion bombardment

It has been shown by Profijt *et al.* that UV radiation and ions from the plasma can damage the film in some cases. When the plasma is ignited, very quickly, a so-called sheath is formed:³ the electrons can reach the chamber walls or any objects placed in the plasma much quicker than the ions. Hence, a region with more ions than electrons is created near all grounded surfaces. Positive ions are accelerated toward the surface when they enter this region. This acceleration can lead to ion energies of several tens to hundreds of electron volts,⁴ which is sufficient to cause considerable damage to the films, or at least physically change them.^{5,6}

One form of ion-induced damage to films comes into the form of film delamination and the formation of bubbles, sometimes referred to as blisters. Caused by compressive stress, these unwanted features have been a long-known issue in the deposition and processing of thin films. In the context of physical vapor deposition, a similar phenomenon is known as atomic peening:^{4,7,8} recoiled Ar atoms impinge on the substrate, resulting in a denser film and increased compressive stress.

Other observations of bubble (or blister—we will use the terms interchangeably) formation in ALD layers were made during an annealing of thermally deposited ALD films. However, in this case, film damage was linked to residual *tensile* stress, and the release of trapped hydrogen, leading to the formation of H₂O and H₂ gas. Then, the barrier properties of Al₂O₃ prevent this gas from diffusing out of the film.^{9–12} Exposure of multilayers to hydrogen neutrals and/or ions leads to blistering in a similar way.¹³ In the case of Al₂O₃, a higher deposition temperature can be used to decrease the number of hydrogen atoms and thus reduce internal stress¹⁴ to avoid blistering.¹⁵ Another known case of blister formation is during ALD growth of noble metals such as the ALD of ruthenium¹⁶ and iridium.¹⁷

Ion bombardment during ALD has also been used as a way to tune material properties (e.g., for the deposition of Ga₂O₃, TiO₂, and ZnO).^{18–22} Over the past few years, substrate biasing has received increasing attention, and for good reason: by biasing a substrate, it is possible to increase the energy of the ions reaching it. The concept of atomic layer annealing as described by Shih

et al.,²³ where the annealing effect from an Ar plasma greatly influences the crystal phase of AlN, shows as well that the energy and momentum transferred from a plasma can strongly alter film properties. These papers demonstrate that the energy and bombardment of these impinging ions could be used to tailor material properties. However, one should realize that this effect is inherently not conformal and it adds another layer of complexity to the system. Therefore, the topic of substrate biasing is considered out of scope, but hopefully, the interested reader will find the ion measurements in Sec. III B of value.

2. Conformality

It often proves hard or impossible to coat challenging (3D) substrates in a conformal way with a PEALD process.^{24–26} The aspect ratio (AR) is defined as the depth of a feature over its width, if necessary with a correction factor to compare different geometries.²⁷ The main reason PEALD processes fail to coat deep inside high-aspect ratio structures is that the activated species, created by the plasma, recombine at the surface. The higher the aspect ratio of the structure, the higher the probability that after a number of collisions with walls, activated species have recombined into nonreactive species. This depletion of reactive species results in nonconformal growth. If we define $\Psi_{\text{full coating}}$ as the number of precursor molecules necessary to conformally coat a feature, for thermal processes, it can be shown that $\Psi_{\text{full coating}} \propto AR^2$ in the diffusion-limited regime, while for plasma-enhanced processes, it becomes exponentially harder to coat high-aspect ratio structures [$\Psi_{\text{full coating}} \propto \exp(AR)$].²⁵ Facing this challenging problem, it should be the aim to maximize the yield of active species near the entrance of a high-aspect ratio structure, in order to upscale PEALD in an economically attractive fashion.

3. Heuristic parameter selection

The use of PEALD as a key enabler for several technological breakthroughs demonstrates its potential, but fundamentally, the properties of the plasma itself and the impact of plasma parameters on the deposited film and its saturation behavior are much less understood. If PEALD is used on a specific tool with a fixed plasma source and little room to play around with positioning or substrate biasing,²⁰ only a few process parameters can be controlled: the flow and pressure in the chamber (which are obviously related but not equivalent), the gas mix, and the plasma power. These parameters are described in more detail in Sec. S1 in the supplementary material.²⁸

Often, a heuristic approach is taken when choosing process parameters, relying on prior experience and parameters used for other processes. Given the fact that plasma-enhanced processes may saturate very quickly on planar substrates, often this is sufficient for process development. Still, changing pressure, flow, or power may change the properties of the plasma and hence change the yield of active species or ion flux toward the substrate.

It is partly understood how these process parameters affect the ion energies. Very interesting and inspiring work has been done by Boris *et al.* and Wheeler *et al.* but their work was mainly directed toward control of ion fluxes.^{21,22,29} In contrast, the creation of reactive species that contribute to the deposition is often overlooked.

Tinck and Bogaerts have simulated an inductively coupled oxygen plasma in a pump-type reactor geometry, in relevant pressure and power ranges³⁰ and determined fluxes for different substrate geometries. The plasma is described well but it is difficult to draw practical recommendations from this modeling effort.

B. Oxygen plasma species

In this work, oxygen plasmas are used. As mentioned before, the addition of energy to the gas by igniting a plasma creates new, reactive species, and because of the electric fields generated, charged species can hit the substrate surface with large energies. In a first-order approximation, these species are created by electrons hitting gas molecules. As the electron temperature changes, the rate coefficients for certain processes change along.²¹

The species generated in the plasma include ions (O_2^+ , O^+ , O_2^- , and O^-) and atomic oxygen (O). Neutral but metastable excited molecular and atomic oxygen might as well be present in significant concentrations.

In PEALD, growth during the plasma step is usually attributed to the creation of radicals and their chemical interaction with the surface groups. Atomic oxygen would be a good candidate as the main driver for surface reactions and also singlet delta oxygen ($^1\Delta_g$), an excited molecular oxygen species with a long lifetime and increased reactivity toward organic groups cannot be excluded.

On the other hand, we consider the main contribution of the ions (O_2^+ , O^+ , O_2^- , and O^-) as physical: they do not contribute to the growth in a chemical sense but the energy they bring to the surface may significantly change the film properties.⁶

C. Paper outline

By now, we have defined three challenges for the PEALD practitioner in the field: controlling damage to the films by ion bombardment, optimizing conformality, and building a better understanding of the effect of plasma source or reactor parameters to species generation in the plasma. In Sec. S1 in the supplementary material,²⁸ we define power, pressure, and flow as relevant plasma parameters for PEALD. By investigating how these parameters affect oxygen plasma properties, effectively tackling the problem of how to select suitable plasma parameters, we can possibly gain an understanding of causes and mitigations for the ion bombardment and conformality problems along the path. A schematic overview of the system under study together with characterization techniques can be found in Fig. 1.

First, we will scan the relevant parameter space (Fig. 2) with optical emission spectroscopy, probing the plasma region. This will provide a basic insight into how power, pressure, and flow affect the generation of atomic oxygen (O) and positive molecular ions (O_2^+) in the source region.

In a second part, we will study the remote region with an electrostatic quadrupole plasma (EQP) analyzer. This allows us to study the flux and energy of O_2^+ , O^+ , O_2^- , and O^- ions that effectively reach the sample substrate in the relevant parameter space.

Finally, these measurements are related with actual depositions. The physical effect of ion bombardment is linked to a series of Al_2O_3 samples deposited at different pressures, while the change in concentration of chemically reactive species with plasma power

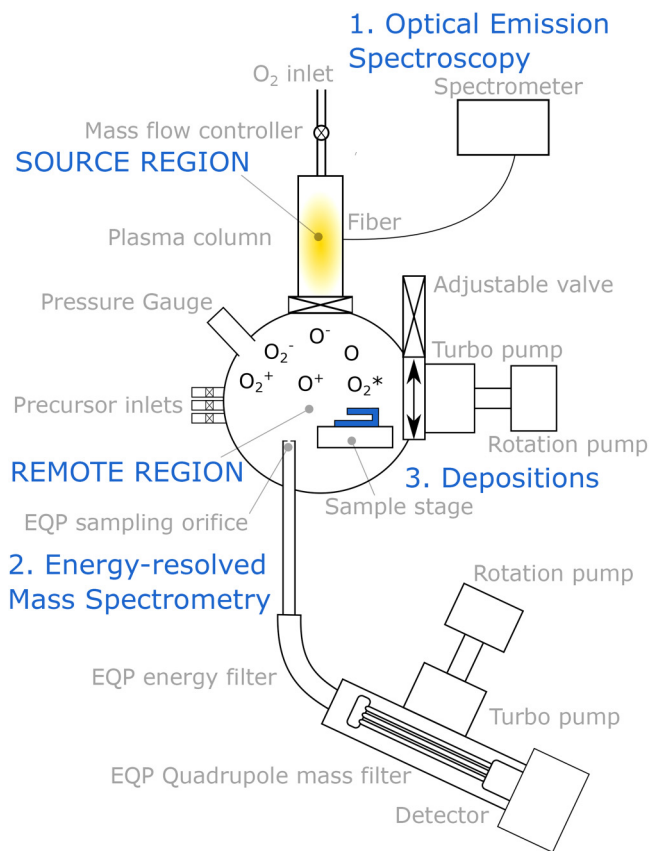


FIG. 1. Schematic diagram of the ALD reactor with plasma source and measurement techniques, serving as a summary of this work. In reality, the EQP device and the sample stage are situated on the axis of the plasma column in the two vacuum systems used for this work.

and pressure is addressed through a series of depositions in lateral high-aspect ratio (LHAR) structures.

II. EXPERIMENT

A. Reactors and plasma source

All depositions were performed in a home-built, cold-wall, vacuum-type ALD reactor with remote inductively coupled plasma (denoted ALD in Table 1). Ion energy measurements were done with a Hiden EQP1000 tool in a dedicated, cubic chamber (denoted EQP in Table 1). The inner dimensions of this chamber were $50.0 \times 50.0 \times 50.0 \text{ cm}^3$. The EQP inlet was located 27 cm from the top of the chamber, right below the plasma tube. A metal cylinder with a diameter of 25.0 cm was placed into this chamber to confine the plasma and to mimic the typical ALD chamber geometry. At the bottom of this cylinder, below the EQP entrance, regularly spaced holes were drilled to imitate the effect of pumping below the sample stage. The turbo pump itself could be screened with a variable gate valve with an action of 26.0 cm. This way the

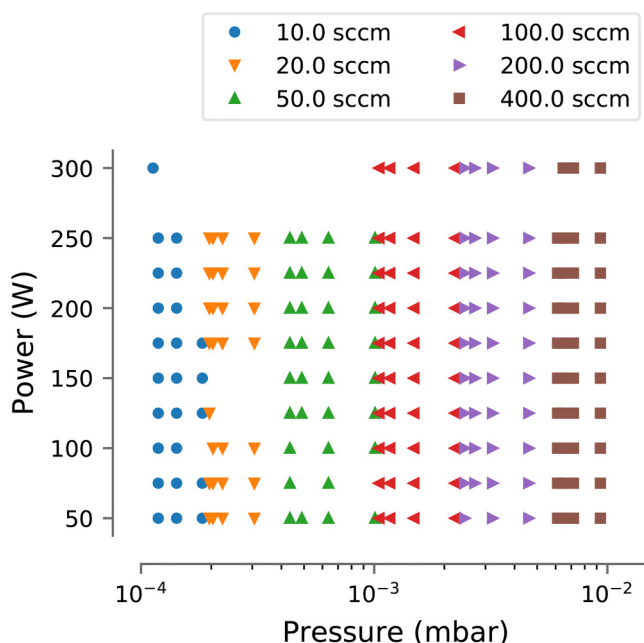


FIG. 2. Optical emission spectroscopy (OES) parameter space explored in this work. Each marker represents an OES spectrum of the plasma integrated for at least 50 s. The flow and the power were controlled in four different experiments, each experiment with a different closing of the gate valve (0 cm or completely open, 10, 15, and 20 cm). This way, one flow can lead to different pressures, indicated by markers of the same color. The total action of the gate valve was 26 cm (completely closed). Missing points indicate where no correct matching happened. For lower pressures, the power was limited to 250 W.

effective pumping speed could be controlled. Oxygen gas entered the chamber from the top of the plasma column with a mass flow controller (MKS 400 sccm, N₂ rated) controlled by an MKS 247C four-channel readout. The RF generator and plasma column from the ALD chamber were used on this system as well. Automated control of the experimental parameters was done with a National Instruments USB-6008 module.

For all experiments, we used the same plasma tube, coil, cables, and generator (Advanced Energy Cesar 136, 13.56 MHz).

An automatic matching unit was used, and so for all measurements, the reflected power was 0 W. The plasma setup was moved between the EQP characterization tool and the ALD reactor. At all times, the pressure was allowed to stabilize before the plasma was ignited.

B. Optical emission spectroscopy

OES measurements were performed with a fiber coupled Ocean Optics QE65000 spectrometer both on the ALD reactor and the EQP chamber with the fiber attached perpendicular to the plasma coil, aimed at the center of the plasma. It was verified that trends observed in the reactor were identical compared to those observed on the EQP system. The integration time was set to 1 s but afterward all spectra recorded within the same regime were averaged to increase signal-to-noise ratio, after subtraction of a background spectrum. Plasma emission did not change significantly over time in the same pulse. Minor changes occurred when the plasma was pulsed very long (more than 60 s), but internal differences were at least an order of magnitude smaller than differences between spectra taken at different conditions. As for higher flows and powers, the emission peak at 777 nm was too intense and saturated the detector in some parts of the parameter space, the region 762–792 nm was left out of the calculation of the total number of counts (for all spectra). The peaks were integrated without subtraction of the broad background contribution of the plasma.

Additional infrared optical emission spectra were obtained under similar circumstances on the EQP chamber with an Avantes Avaspec-NIRS512-1.7-HSC-EVO (900–1700 nm). In this experiment, plasma pulses of 10 s were given for a range of powers and flows.

C. Electrostatic quadrupole plasma

The Hiden EQP1000 is a versatile tool that can be used for the detection of neutrals, through electron impact ionization (as demonstrated in, e.g., Ref. 31), or for the direct detection of ions (as, e.g., described in Ref. 32). For EQP sampling, the plasmas need to be maintained for a longer time than a typical ALD pulse time. 60 s pulses of plasma were given with 60 s breaks in between. OES measurements were taken to assure that the plasma conditions were similar to those in the ALD reactor. Because of very high counts at low pressures and detector saturation, we did not study the lowest flows with the EQP experiment. Instead, the 100–400 sccm range

TABLE I. Overview of experiments described in this work with the part of the parameter space they cover.

Technique	Reactor	Flow (sccm)	Pressure (mbar)	Power (W)	Figure
OES	EQP	10–400	1×10^{-4} – 1×10^{-2}	50–300	2 and 6
IR-OES	EQP	10–400	6×10^{-4} – 1×10^{-2}	50–250	5
OES	ALD	n.a.	6×10^{-4} – 1×10^{-2}	20–250	4 and S3
EQP	EQP	100–400	2.3×10^{-3} – 1×10^{-2}	50–250	7 and 8
Depositions	ALD	n.a.	3.5×10^{-4} – 1×10^{-2}	150	9
Depositions	ALD	n.a.	5×10^{-3}	50–200	11
Depositions	ALD	n.a.	6×10^{-4} – 1×10^{-2}	150	12

was studied in steps of 50 sccm. For positive ions, we used an energy step of 0.2 eV, while for negative ions, an energy step of 0.5 eV was used. For all EQP experiments, the valve toward the pump was completely opened. We tried to measure atomic oxygen in several ways with the EQP tool in the residual gas analysis (RGA) mode, threshold ionization mass spectrometry (TIMS), and the negative RGA mode. However, the signal-to-noise ratio of the measurements was insufficient due to the high background signal of dissociation of oxygen in the ionization source for RGA, and the relatively low sensitivity and ionization cross sections of TIMS measurements for low-pressure high-energy species.

D. Depositions

All films referenced in Sec. III C were deposited with 200 cycles of TMA-O₂* at 120 °C substrate temperature. Trimethylaluminum (TMA) (Strem, 97%) and O₂ (grade 5.0, 99.999% pure) were used for the depositions. A cycle consisted of 5 s of TMA at 2×10^{-3} mbar, followed by 30 s of pump time. The oxygen pulse consisted of 5 s of gas flow in order to stabilize the pressure (which was varied from 3.5×10^{-4} to 1.0×10^{-2} mbar), followed by 5 s of plasma power, again 5 s regular gas flow, and concluded by a 30 s pump step. The plasma power used for all depositions was 150 W. O₂ was inserted directly in the reactor for the depositions shown in Fig. 9. A similar experiment was performed with the gas inlet at the top of the plasma column.

For the conformality analysis, we performed two sets of depositions. A first set consisted of six depositions with 200 cycles of TMA (9 s, 5×10^{-3} mbar) and oxygen plasma (variable pulse length, 5×10^{-3} mbar) in a macroscopic, lateral trench (Fig. 3) with opening height 1 mm, width 10 mm, and depth 20 mm, resulting in an aspect ratio of 20 and an equivalent aspect ratio of 10.^{27,33} The deposition temperature was 100 °C. The second set consisted of five depositions with 200 cycles of TMA (5 s, 5×10^{-3} mbar) and oxygen plasma (5 s plasma pulse length,

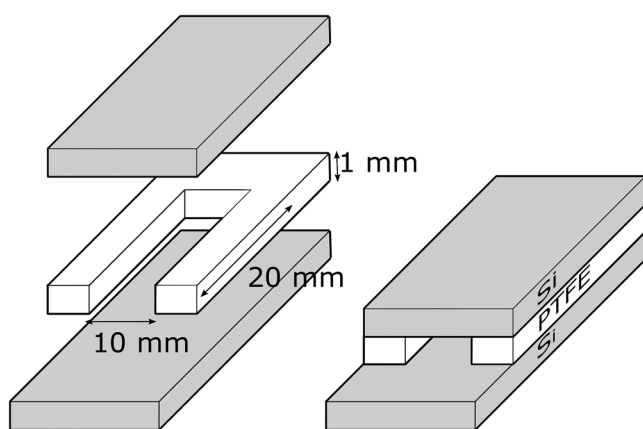


FIG. 3. Schematic view, exploded and assembled, of the macroscopic test structures used. Stacking two pieces of Si with a polytetrafluoroethylene (teflon) spacer in between results in a laterally oriented, rectangular hole.

150 W, variable pressure) in the same trench structure with a deposition temperature of 120 °C.

The excess TMA dose delivered should be sufficient to ensure that the deposition profile is determined by the oxygen plasma step. After deposition, the thickness profiles were measured with a mapping ellipsometry setup with one datapoint every millimeter (Figs. 11 and 12). The thickness was normalized assuming a saturated thickness of 22 nm (200 cycles with a growth per cycle of 1.1 Å).

The film thickness was measured with a J.A. Woollam F2000 spectroscopic ellipsometer; and blister formation was studied with an FEI Quantafeg SEM.

E. Simulation and fit of deposition thickness profiles

The simulation and fit of deposition thickness profiles were done using a Markov chain approach described elsewhere.³⁴ We implemented our own version of this algorithm. A comparison to the original code can be found in the supplementary material.²⁸ The simulation relies on transmission probabilities: when a particle collides at depth z_1 , the probability of its next collision can be calculated as a function of z , assuming cosine re-emission and the view factors for the geometry under study. The transmission probabilities were calculated for a square hole,³⁵ although the simulation itself was performed in 1D. The equivalent aspect ratio of this hole was 10, to be able to compare the simulated profile with the deposition thickness profile. Sometimes, a slight thickness increase has been reported at the bottom of the deposition thickness profile, although this was not observed here. Hence, to model the bottom segment, instead of diffuse cosine re-emission, specular reflection of particles was assumed.

III. RESULTS AND DISCUSSION

A. Plasma region: Optical emission spectroscopy

Optical emission spectroscopy is sometimes, but not often, used in ALD research to investigate reaction products during the plasma pulse.³⁶ Here, it is used as a tool to study the plasma itself. The addition of an actinometer gas such as Ar was considered and rejected, as the main interest was to probe the pure O₂ plasma as used in ALD configurations, and it has been shown that the addition of Ar plasma may change the film and plasma properties.³⁷ As a result, only qualitative conclusions will be made.

1. Components of the spectrum of oxygen plasma

Some optical spectra, obtained by varying the power at a fixed pressure, are plotted in Fig. 4. Qualitatively, all spectra are very similar. By plotting on a log scale, a lot of features can be seen. Atomic components can be mapped using Grotrian diagrams,³⁸ which are compiled in Ref. 39, while the molecular spectra of O₂ and ions have been compiled by Krupenie.⁴⁰ A general resource for the identification of molecular lines is supplied by Pearse and Gaydon.⁴¹

Singlet delta (¹Δ_g) molecular oxygen might as well be of interest for ALD. Because this excited molecular oxygen is metastable, it is hard to detect optically due to its low Einstein coefficient $A' = 2.58 \times 10^{-4} \text{ s}^{-1}$. This leads to a very long lifetime (ultimately depending on the gas pressure)⁴² but it is very reactive toward

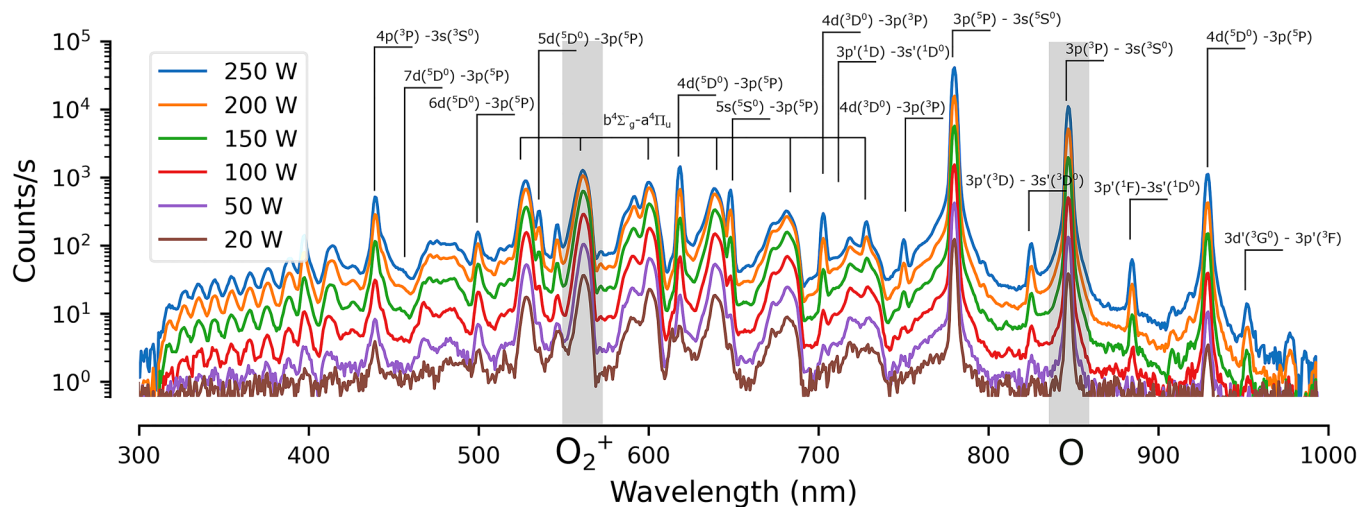


FIG. 4. Spectra of the plasma at different powers on an ALD reactor, and a fixed pressure of 2×10^{-3} mbar. The y axis is logarithmic to show all features. A list of transitions is compiled in the supplementary material.²⁸ The gray zones indicate the zones used for integrating the counts for molecular ions (O_2^+ , 547–566 nm) and atoms (O, 840–850 nm). A similar figure where the power is kept constant and the pressure is varied can be found in Fig. S3 in the supplementary material.²⁸ The peaks at the left (between 300 and 400 nm) are due to the $A^2\Pi_u - X^2\Pi_g$ molecular ion system.

organic groups. The energy difference between the $^1\Delta_g$ state and the ground state of molecular oxygen is 0.98 eV or 1265 nm. Krupenie mentions additional optical transitions at 1067 nm and possibly as well at 924 and 1580 nm due to vibrational levels.⁴⁰ Preliminary infrared emission spectra were collected for a range of flows and pressures. Peaks at 1265 and 1067 nm were indeed observed (Fig. 5). However, these peaks seem to be self-absorbing because of neutral O_2 molecules that get excited into the metastable state upon catching a photon with the right energy. This renders integrating the peaks, as performed in III A 2 for the other species, impossible. In contrast, the detection of these peaks shows that

metastable $^1\Delta_g$ molecular oxygen might as well play an important role in ALD growth.

We identify lines of atomic oxygen (O) in singlet, triplet, and quintet configurations, and lines of molecular ions O_2^+ (first and second negative systems). No clear signs of O_2 , O^+ , O_2^- , or O^- emission were found.

To study the trends in intensity for O and O_2^+ , a typical transition was selected for each. The peak caused by the triplet $3p^3P - 3s^3S^0$ transition at 844 nm was integrated for the atomic O, and for the molecular ion O_2^+ , the peak around 560 nm was integrated. These zones are indicated in Fig. 4.

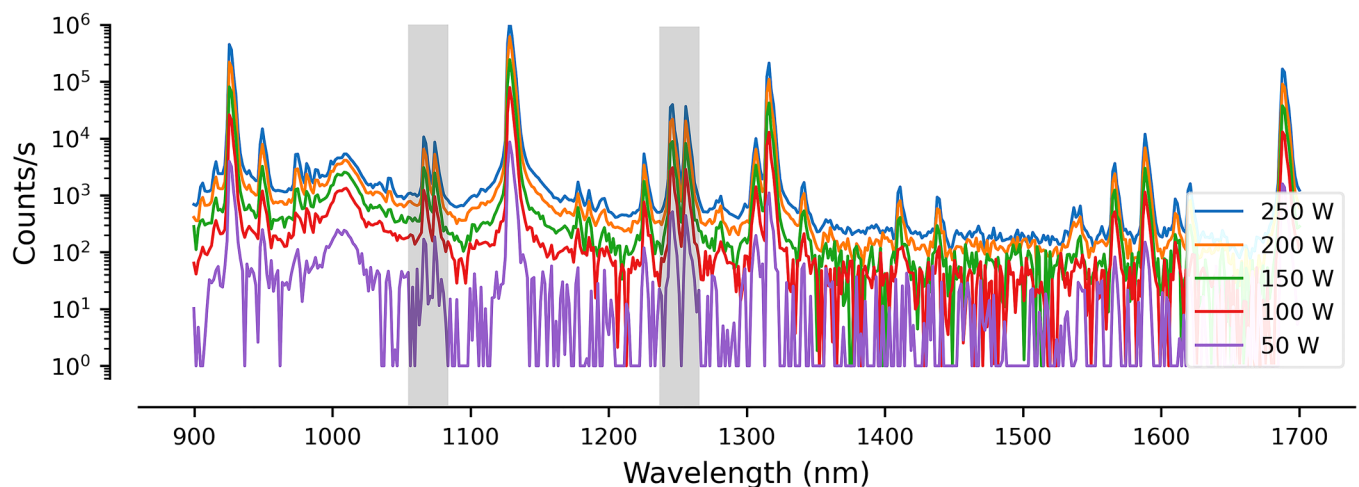


FIG. 5. Infrared spectra at different powers and a flow of 200 sccm. The self-absorbing $^1\Delta_g$ regions are indicated in gray.

2. Trends in OES spectra

When interpreting OES results, the following relationship relates an observed line intensity to the amount of species in the excited state p :⁴³

$$I_{pk} = n_i(p)A_{pk}, \quad (1)$$

with I_{pk} being the intensity of the line that corresponds to the radiative de-excitation of a plasma species i (with density n_i) from an upper level p to a lower level k . The factor A_{pk} is the Einstein coefficient, which determines the probability of this transition. Hence, on the one hand, we can define a depopulation process for $n_i(p)$ as

$$\left[\frac{\partial n_i(p)}{\partial t} \right]_{\text{radiative}} = n_i(p) \sum_k A_{pk}. \quad (2)$$

On the other hand, several mechanisms may contribute to the population of the energy level p . First, we consider the creation of the species i , either in ground state or in excited state p , through electron interactions,

$$\left[\frac{\partial n_i}{\partial t} \right]_{\text{creation from } n_0} = n_e n_0 X_{0i}^{\text{cre}}(E_e, \nu), \quad (3)$$

with n_e being the electron density, n_0 the neutral gas density, and $X_{0i}^{\text{cre}}(E_e, \nu)$ the rate coefficient of the creation process (in $\text{m}^3 \text{s}^{-1}$), which depends on the electron energy distribution or (if it can be defined) the electron temperature. Furthermore, vibrational excitations of the parent molecule ν may as well heavily impact the rate coefficients. Examples of the electron-mediated creation mechanism for an O_2 plasma are direct electron ionization and dissociation processes and also dissociative electron attachment.⁴⁴ Species can be created in the ground state or in an excited state p , in particular, excited O through dissociative attachment.

Other similar creation pathways exist through electronic interaction with other plasma species j ,

$$\left[\frac{\partial n_i}{\partial t} \right]_{\text{creation from } n_j} = \sum_{j \neq i} n_e n_j X_{ji}^{\text{cre}}(E_e). \quad (4)$$

For oxygen plasma, nonelectronic interactions can as well have large rate coefficients, for example, the $\text{O}^+ + \text{O}^- \rightarrow \text{O} + \text{O}$ or $\text{O}_2 + \text{O}$ interactions. This results in

$$\left[\frac{\partial n_i}{\partial t} \right]_{\text{non-electronic creation}} = \sum_{j \neq i} \sum_{k \neq i} n_j n_k X_{jk}^{\text{cre}}, \quad (5)$$

where the resulting species can again be in the ground state or in the excited state. The latter may be favorable given the chemical energy released in these interactions.⁴⁵

Finally, we consider populating the level p from lower lying levels k of the same species i through electronic excitation

$$\left[\frac{\partial n_i(p)}{\partial t} \right]_{\text{excitation}} = n_e \sum_{k < p} n_i(k) X_{kp}^{\text{exc}}(E_e). \quad (6)$$

The mechanisms listed above are not all possible mechanisms. We have neglected depopulation processes such as nonradiative de-excitation pathways, wall interactions, and pumping. This is possible when electron densities are sufficiently low. In steady-state conditions, the total $\left[\frac{\partial n_i(p)}{\partial t} \right]_{\text{total}} = 0$ and the mechanisms listed are sufficient to interpret the observed trends.

The integrated O and O_2^+ peaks as well as the total intensities of the optical spectra scale in a quadratic way with power (Fig. 4), but only a limited effect of pressure and flow on the total intensity is observed. This can be explained by assuming a linear increase of n_e , n_{O} , $n_{\text{O}_2^+}$, and other plasma species with plasma power. The increase in density of plasma species n_i along with the electron density n_e follows directly from Eq. (3). However, the optically observed lines are proportional to the excited species density $n_i(p)$. For oxygen plasma, both electronic and nonelectronic processes might play a role. The relevant contributions to the steady-state population and depopulation processes are Eqs. (2), (5), and (6), leading to

$$I_{pk} = n_i(p)A_{pk} \quad (7)$$

$$\propto \left[\frac{\partial n_i(p)}{\partial t} \right]_{\text{radiative}}, \quad (8)$$

$$\left[\frac{\partial n_i(p)}{\partial t} \right]_{\text{radiative}} \approx \left[\frac{\partial n_i}{\partial t} \right]_{\text{non-electronic creation}} + \left[\frac{\partial n_i(p)}{\partial t} \right]_{\text{excitation}} \quad (9)$$

$$= \sum_{j \neq i} \sum_{k \neq i} n_j n_k X_{jk}^{\text{cre}} + n_e \sum_{k < p} n_i(k) X_{kp}^{\text{exc}}(E_e) \quad (10)$$

if n_e , n_i , n_j , and n_k scale linearly with the power; this explains the quadratic behavior of the intensity of the spectrum with the power. The proportionality indicates that a level p might decay radiatively to multiple other levels, and the approximation symbol indicates that only the main terms are taken into account.

The effects of flow and pressure are harder to pinpoint. To study trends in the creation and excitation rate coefficients $X(E_e)$, it is instructive to normalize the integrated intensity for the selected ionic and atomic peak by the total intensity of the spectrum. This way, the quadratic effect is removed.

These normalized intensities are shown in Figs. 6(c) (O_2^+) and 6(d) (O). As the power and the flow increase, the ionic fraction decreases, and the atomic fraction in the spectrum increases.

Creation rate coefficients for the different processes were obtained from the work of Gudmundsson:⁴⁶ for molecular ions $e + \text{O}_2 \rightarrow \text{O}_2 + e$, the rate coefficient increases with increasing electron temperature: $2.34 \times 10^{-15} \times T_e^{1.03} \times \exp(-12.29/T_e) \text{m}^3 \text{s}^{-1}$. For neutral atoms, two processes contribute to their creation: for $e + \text{O}_2 \rightarrow \text{O} + \text{O}^-$, the creation rate coefficient

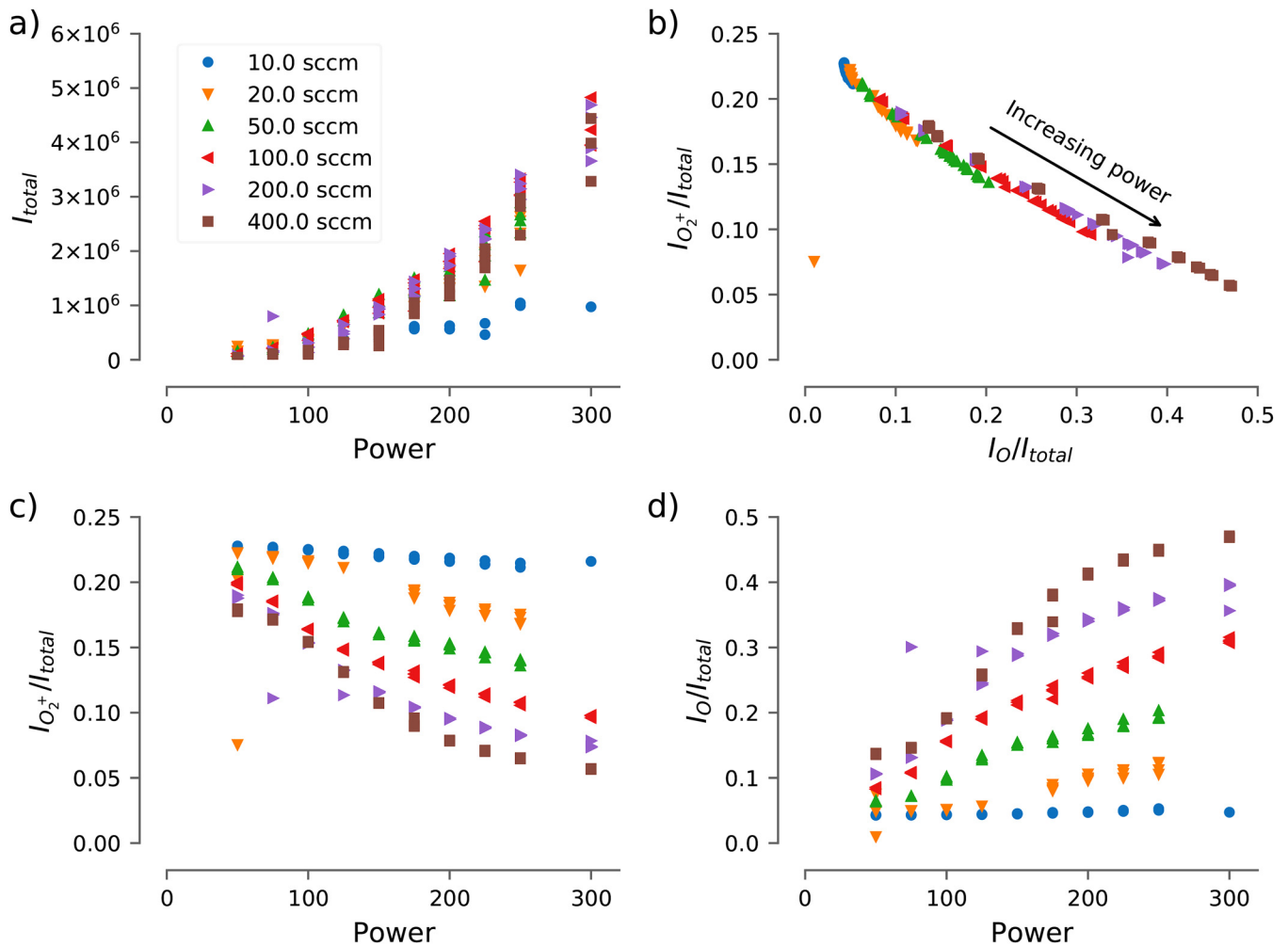


FIG. 6. (a) Total intensity as a function of plasma power. A quadratic relationship appears. Given the size of the parameter space, it is remarkable how similar the total intensity values are. (b) Universal trend for scaled atomic and ionic intensities. (c) Intensity of the ionic line at 547–566 nm, scaled with the total intensity without the saturated line. High flow and high power seem to reduce the ionic fraction in the plasma. (d) Intensity of the atomic line at 840–850 nm, scaled with the total intensity. High flow and high power seem to increase the atomic fraction in the plasma. These data are presented in different ways in Figs. S4 and S5 in the supplementary material.²⁸

is $1.07 \times 10^{-15} \times T_e^{-1.39} \times \exp(-6.26/T_e) \text{ m}^3 \text{ s}^{-1}$ and for $e + \text{O}_2 \rightarrow \text{O} + \text{O} + e$, the creation rate coefficient is $1.41 \times 10^{-15} \times T_e^{0.22} \times \exp(-12.62/T_e) \text{ m}^3 \text{ s}^{-1}$. This leads to a net decrease in O production with increasing electron temperature.

$\left[\frac{\partial n_i}{\partial t}\right]_{\text{non-electronic creation}}$ is only dependent on the gas temperature and the respective densities of O_2^+ , O^+ , and O^- . $\text{O}^+ + \text{O}^- \rightarrow \text{O} + \text{O}$ has a rate coefficient of $4.00 \times 10^{-14} \times (300/T_g)^{0.43} \text{ m}^3 \text{ s}^{-1}$ and $\text{O}_2^+ + \text{O}^- \rightarrow \text{O}_2 + \text{O}$ has a rate coefficient of $2.60 \times 10^{-14} \times (300/T_g)^{0.44} \text{ m}^3 \text{ s}^{-1}$.

Hence, from the decrease in ionic fraction as opposed to the increase in atomic fraction with increasing flow, we infer that, at least for an oxygen plasma, increasing the flow leads to a decreased electron temperature [Fig. 6(b)]. A similar effect can be seen with

the power: an increased power leads to a decreased electron temperature.

From this, it follows that the ratio $\frac{[\text{O}]}{[\text{O}_2^+]}$ is inversely proportional to the electron temperature. At high power and high flow, the electron temperature will be lower and the relative fraction of oxygen atoms will be higher (despite the creation of more electrons and in general more plasma species at higher powers), while at low power and low flow, the relative fraction of ions will be higher.

The effect of pressure on the atom-to-ion ratio is only minor: in Fig. 6, the data from all spectra with all valve positions are plotted, varying the pressure while maintaining the same flow. It can be seen that the effect of variations in flow is much larger. This might not immediately catch attention, as the points obtained at

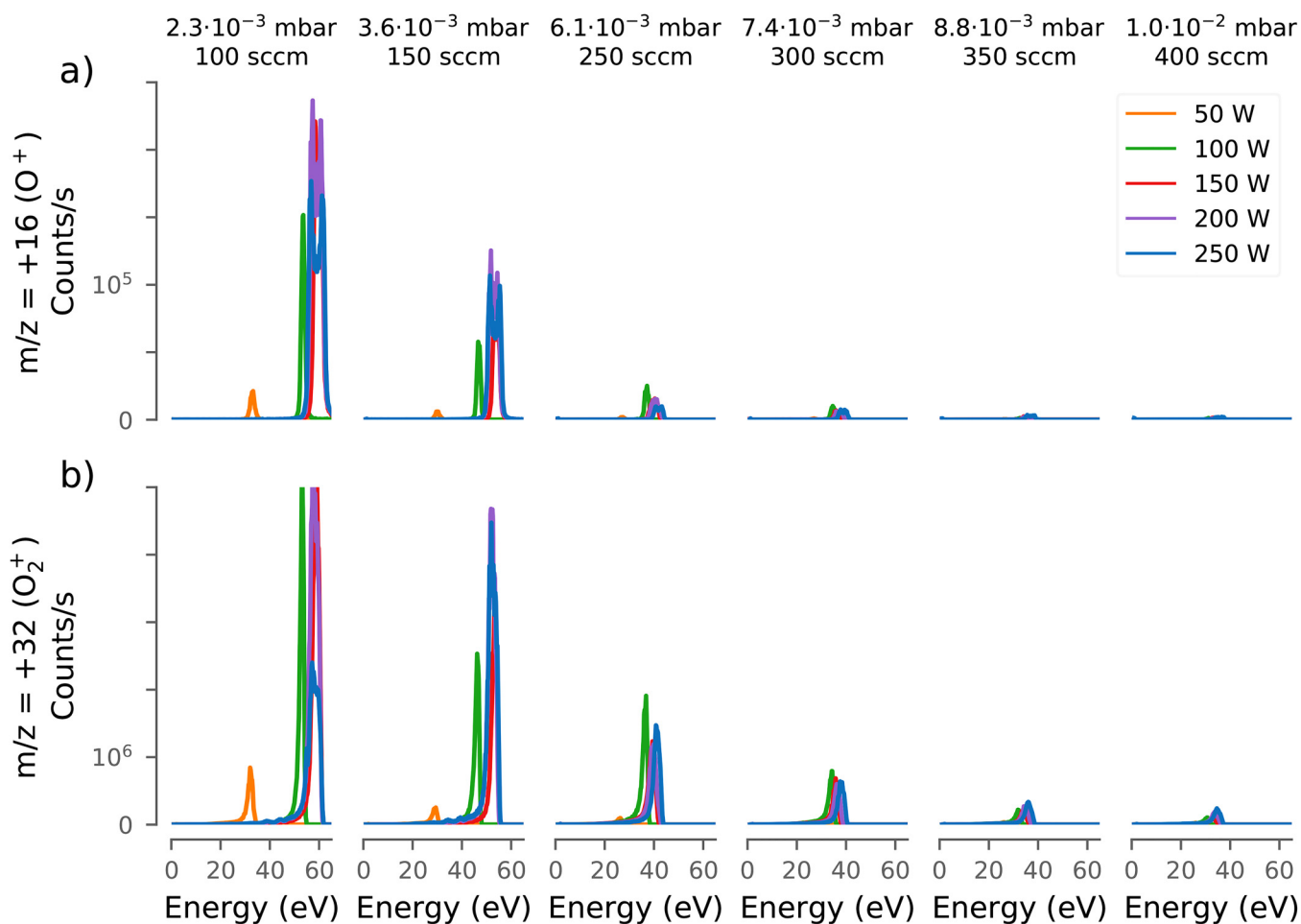


FIG. 7. Energy spectrum for the incoming ions as a function of pressure (by increasing the flow) and power. (a) Distributions for atomic, positive ions (O^+) (b) for molecular, positive ions (O_2^+). For all species, a dramatic decrease in ion flux can be observed with increasing pressure. Spectra collected for powers 75, 125, 175, and 225 W confirmed the trends but were omitted for the sake of clarity.

the same flow are plotted on top of each other. Slices at 200 W are provided in Fig. S4 in the supplementary material.²⁸ As mentioned before, in the absence of a valve to control the pumping speed, increasing the flow will result in an increased pressure as well.

During the experiments, it was observed that the plasma region became visibly smaller with increasing pressure, probably due to increased nonradiative decay processes at higher pressures. This is not visible in these graphs, as we measured at the center of the coil, although this effect is somewhat visible in Fig. S5 in the supplementary material.²⁸

At this point, a preliminary conclusion can be made, based on OES measurements at the center of the plasma region: the concentrations or partial pressures of dissociated species (via detection of atomic O) and ions (via detection of molecular O_2^+) both increase in a linear way with the power. The ratio between these two partial pressures is determined by the electron temperature, mediated by

the flow, and the plasma power. As such, higher flows and powers lead to a higher atom-to-ion ratio, while the absolute number of both O and O_2^+ is mainly determined by the power.

n_e and T_e are peaked in the center of the plasma, which is the reason this is the brightest region. However, the density of other plasma species can stretch far beyond the plasma region, as the effective use of remote plasma for ALD readily suggests. This is why in Secs. III B–III D, we will investigate the plasma species in the remote zone.

B. EQP measurements: ions in the remote region

Ion energy distribution functions were measured with an EQP. We discern four kinds of ions: atomic, positive ions (O^+), molecular, positive ions (O_2^+), atomic, negative ions (O^-), and molecular, negative ions (O_2^-). The distributions (shown in Figs. 7 and 8) show

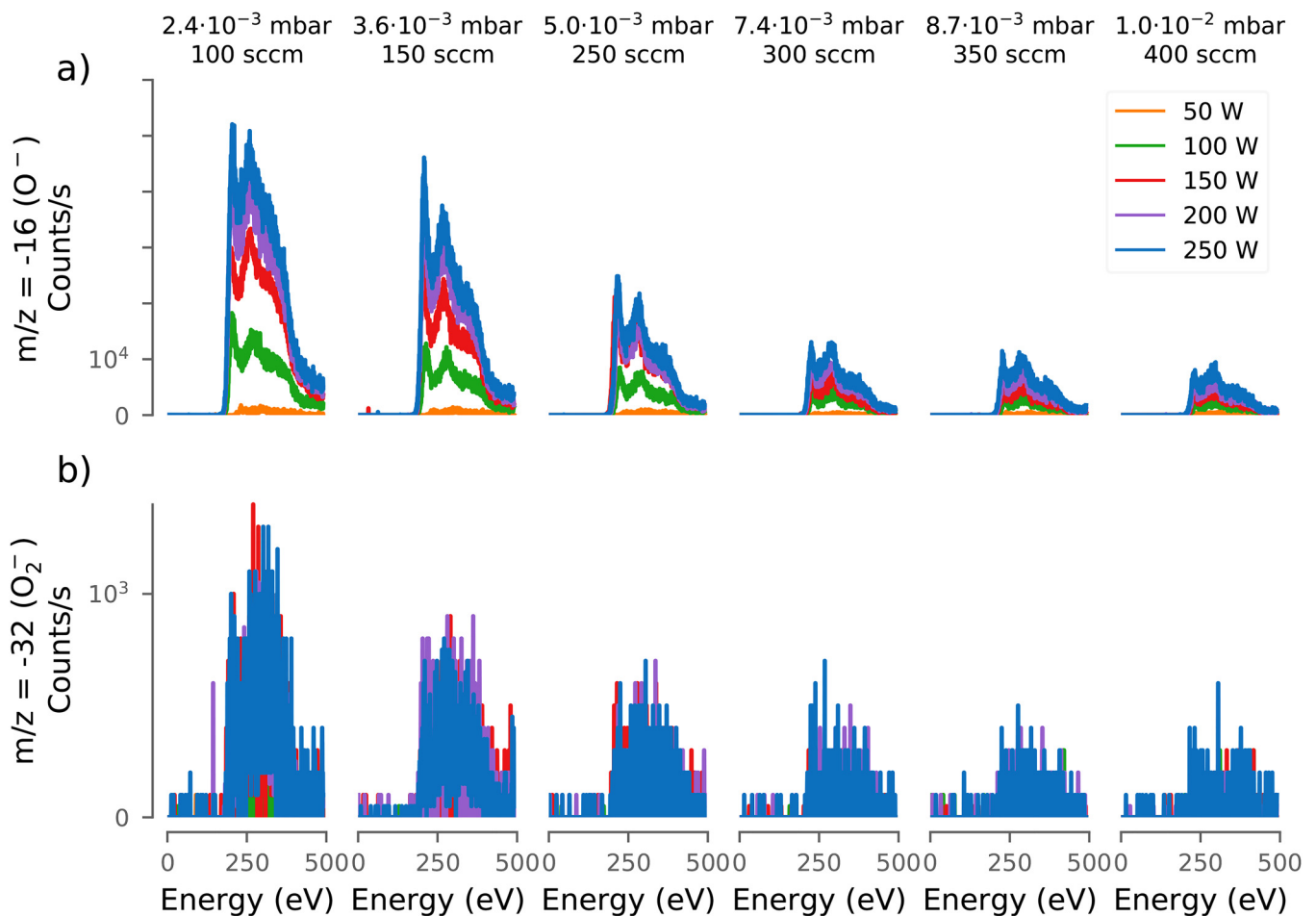


FIG. 8. Energy spectrum for the incoming ions as a function of pressure (by increasing the flow) and power. (a) Distributions for atomic, negative ions (O^-) and (b) molecular, negative ions (O_2^-). For all species, a dramatic decrease in ion flux can be observed with increasing pressure. Spectra collected for powers 75, 125, 175, and 225 W confirmed the trends but were omitted for the sake of clarity.

several general trends: a higher power always results in more ions, but with higher pressure, less ions reach the sampling orifice (at the substrate position). This can be attributed to an increased collision probability (with subsequent neutralization) and thus a shorter mean free path toward the surface at higher pressures.

Below 150 W, the plasma potential, equal for O^+ and O_2^+ , seems to increase with increasing power (Fig. 7). For powers above 150 W, the plasma potential remains constant with power between 40 and 60 eV, depending on the pressure. For positive ions, higher intensities seem to correlate with a higher plasma potential (hence more ions reach the surface with more energy) and the saddle shape characteristic for ion energy distributions in RF plasmas can be observed.

Oxygen, due to its high electronegativity, has the tendency to create electronegative plasmas. Optical transitions are not available for negative species, as the excess electron is removed rather than excited. EQP measurements show that the O^- contribution is

indeed large and spreads out over a wide energy window (0–500 eV) (Fig. 8). Consistent with the modeling results of Tink and Bogaerts,³⁰ the O_2^- contribution is negligible. However, the energies of the negative ions are surprisingly high, and the energy distributions of the negative ions are much broader than those of the positive ions. At this point, we have no explanation for the high-energy values observed. We believe that the general trends observed for negative ions are valid, but we want to stress that further research into the energy distributions of positive and negative ions is necessary, in particular, in seeking an explanation for the high energies for negative ions.

C. Impact of ions on ALD depositions

To test the effect of pressure on deposition quality, two series of Al_2O_3 depositions were performed: in these experiments, all parameters were fixed, except for the gas pressure. In the first

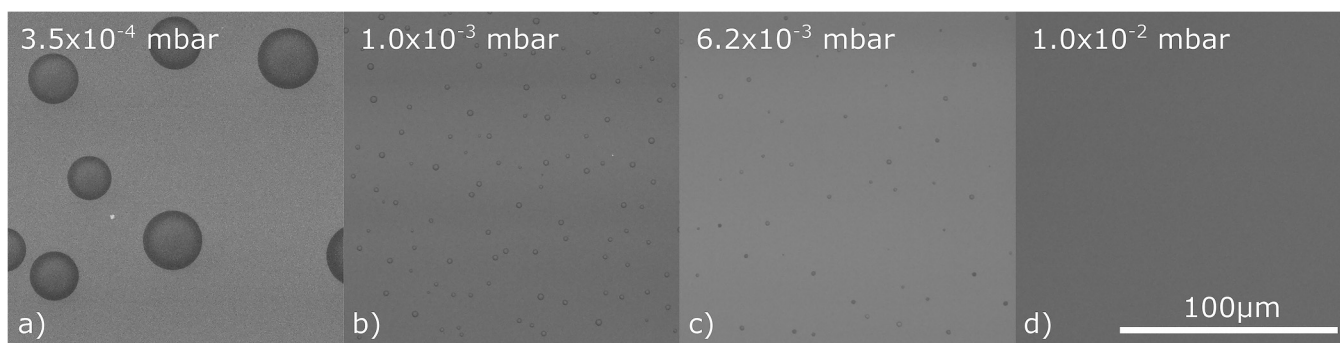


FIG. 9. SEM images of samples grown with varying O_2 pressures but otherwise an identical process (200 cycles TMA- O_2^+ , 150 W). (a) 3.5×10^{-4} , (b) 1.0×10^{-3} , (c) 6.2×10^{-3} , and (d) 1.0×10^{-2} mbar. As the pressure is increased, the amount and the size of the features are decreasing until at 1.0×10^{-2} mbar no bubbles are visible anymore. All images have the same scale.

series, the gas was fed to the top of the plasma column and all gas had to flow through the plasma zone. In the second series, the gas entered the reactor from the side. While in the first series, no visible damage was observed (SEM images not shown), and in the second series, a clear trend in the film damage (damage in the form of bubble formation) could be observed (Fig. 9). We assume that the ion concentrations are even higher when the gas enters the reactor from the side. As the pressure increases, the bubbles decrease in size and/or spacing and ultimately vanish at the highest plasma pressure.

As bubbles are typically an indication of compressive stress, it can safely be assumed that stress in the films is caused by ion bombardment and that this stress can be reduced by an increased pressure. Even if ion-induced effects are not visible as dramatically as in Fig. 9, plasma-induced defects may still alter the film properties. The deposited samples were characterized with x-ray reflectivity and spectroscopic ellipsometry. No significant differences in thickness or density were observed.

We noticed that damage (bubble formation and delamination) only occurred to samples within line of sight of the plasma. Around clamps and inside lateral test structures, the films are usually very smooth and conformal. This circumstantial evidence shows that ions, hitting and damaging the substrate within line of sight, lose their energy (or regain their neutrality) upon the collisions necessary to enter 3D structures. Arts *et al.* have also showed compelling evidence for the fact that ions are not able to enter LHAR structures.⁶ A similar experiment was done with the EQP: it is possible to close a shutter before the sampling orifice. Normally, this shutter is opened for optimal line-of-sight sampling. However, there is still some space in between the shutter and the orifice, and neutral gas species can still be sampled. When the shutter is closed, the number of detected ions goes to zero. This is additional proof of our findings. We expect this only to be of effect if the distance between the overhanging structure and the substrate is smaller than the sheath width. Finally, as we showed, a plain-out increase of the gas pressure also may reduce ion damage and blister formation but UV-induced damage and less drastic defect formation may still be present.

D. Effect of radicals on ALD growth

From the results presented in Sec. III A, we concluded that as the plasma power increases, more species are created in the plasma region. The relationship between power and total species concentration is linear, although relative concentrations might change with increasing power (due to a changing electron temperature). Hence, it would be of interest to see whether the effect of plasma power and pressure on actual depositions can be measured—assuming that only the radicals take part in the growth. This is more subtle than it seems: we work with a remote plasma, so OES measurements in the plasma column cannot necessarily be extrapolated to the sample region. While ions are easily lost through collisions at the walls and gas-phase collisions, atomic species typically are not lost in the gas phase, and the recombination coefficient at the reactor walls is surface-dependent and may be moderate. As ions inherently cannot contribute to conformal growth in a lateral structure (as described in Sec. III C), we will focus in this section on the radical species. For now, it will be assumed that the growth is dominated by atomic oxygen. An obvious technique for following the process would be real-time *in situ* ellipsometry measurements of the thickness, to compare saturation curves as a function of the plasma power. However, here it is rather useless since saturation usually is obtained extremely fast during plasma steps.

Therefore, an alternative way is needed to investigate the effect of plasma power and pressure on actual depositions. No ALD paper is complete without the statement that it is a technique able to *conformally* coat substrates.²⁷ Usually, the saturation curve is reported as a proxy of this statement: if this reaction saturates on a planar substrate, it will as well be able to coat a challenging 3D structure. Here, deposition thickness profiles inside 3D high-aspect ratio structures will be studied as a function of the plasma power and pressure, in order to calculate back the partial pressure of active species at the entrance.

If different plasma conditions result in a higher partial pressure of radicals near the entrance of the structure, the flux ϕ of active species toward the substrate will increase as well (see Sec. S1 in the supplementary material).²⁸ As the plasma species are very

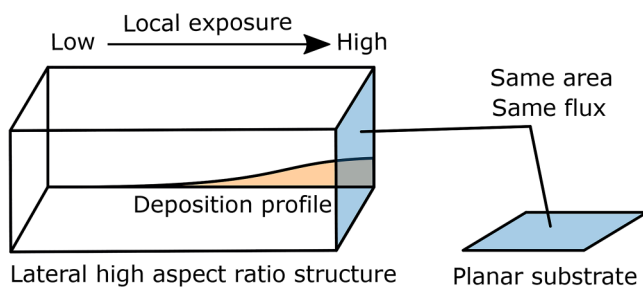


FIG. 10. Lateral high-aspect structure may receive the same amount of flux compared to a planar substrate with the same surface area but has more surface groups. Furthermore, the groups closer to the entrance will receive a higher exposure than those deeper in the structure. This yields a deposition profile that is essentially a saturation graph spread out in space rather than in time.

reactive, very low fluxes will already react with all surface groups. By increasing the effective surface to coat with the same flux, we obtain a very useful characterization device (Fig. 10). The deposition profile can be examined *ex situ*, as it encodes useful information about the process.

However, we need a tool to decode the information that lays hidden in the deposition profile. Conformality modeling started with the seminal work of Gordon *et al.*,⁴⁷ assuming a sticking probability of 1. In the following years, a multitude of analytical and computational models and several simulation techniques were reported. The main aim has been to investigate which exposures are necessary to completely (or almost completely) coat a high-aspect ratio structure, knowing process and precursor characteristics (sticking and recombination coefficient) beforehand.^{48,49} Another section of the literature dealt with these parameters, such as the sticking coefficient, and how they can be determined through the study of certain features (such as the slope) of the deposition profile.^{24,50,51}

Here, we propose to introduce another approach: one elegant way of simulating ALD growth has been through the modeling of the transport and reaction of the process as a Markov chain by Yanguas-Gil and Elam.³⁴ For a given coverage (as a function of depth), it is possible to calculate the reaction probability (again as a function of depth). By treating the changing coverage profile as an initial value problem and repeated evaluation of the reaction probability, it is possible to simulate ALD growth in a HAR structure. The sticking coefficient (for first-order Langmuir adsorption), the recombination coefficient, and the deposition profile as a function of a varying coverage are encompassed in a computationally efficient way.

Until recently, no open source implementation of this simulation approach was available, so we reimplemented the algorithm and benchmarked it to ensure physical validity (see SI).²⁸ However, we aim to go beyond simulation: because of the computational efficiency of the algorithm, we propose it is possible to use a least squares fitting procedure to obtain all experimental information from simultaneously fitting a set of deposition profiles. Hence, it would be possible to derive the common sticking probability and

recombination coefficient for these processes and, most relevant for our case, also the partial pressure at the entrance of the profile that led to each particular profile. By fitting deposition thickness profiles with different plasma powers and pressures, it may be possible to identify relevant trends.

The simulation framework we use requires a feature geometry, a sticking probability, a recombination coefficient, and an exposure Ψ to simulate a conformality profile. To properly scale the results, an area per surface site s_0 is also necessary. On the other hand, the experimental input to fit the profiles needs to be rescaled as well: the deposition thickness profile needs to be divided by the expected thickness to scale back to a conformality profile.⁵² In Sec. S1 in the supplementary material,²⁸ we present a more detailed account of the notation and assumptions made in the simulation. As long as the TMA exposure is oversaturated, we can be sure that the oxygen plasma is limiting the growth. In earlier work, we reported deposition thickness profiles as a function of plasma power in similar structures.²⁴ The pulse times were longer in that case, possibly leading to recombination-limited growth and less difference between profiles at different plasma powers.

Fits to the experimentally obtained saturation thickness profiles are shown in Figs. 11 and 12. The resulting partial pressures at the entrance of the trench can be found in Figs. 13 and 14. All profiles in one set (a set for the power and a set for the pressure) were fitted simultaneously. This means that in the minimization routine for the power-varied profiles, seven parameters were optimized: the sticking probability and six exposures. In the minimization routine for the pressure-varied profiles, six parameters were optimized: the sticking probability and five exposures.

The recombination coefficient was kept constant at the literature value of 0.0021,⁵³ also within the range obtained by Arts *et al.*²⁶ (between 0.01 and 0.001 on Al_2O_3). In principle, it would be possible to vary this parameter as well, but it is important to

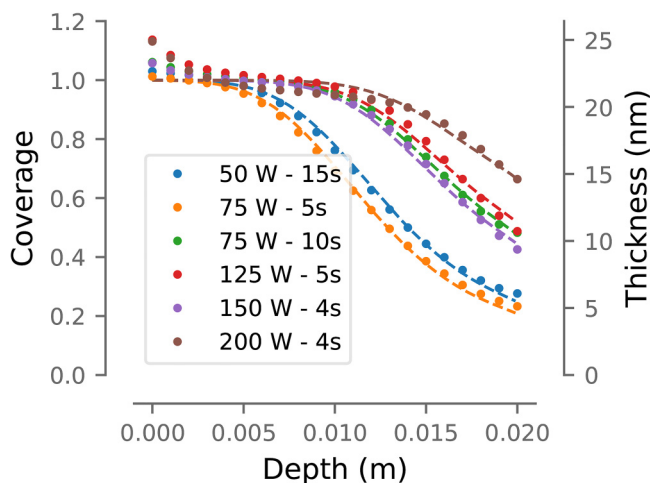


FIG. 11. Normalized deposition thickness profiles (dots) and simulated conformality profiles (lines) for depositions where the power and the pulse time were varied for a fixed pressure of 5×10^{-3} mbar.

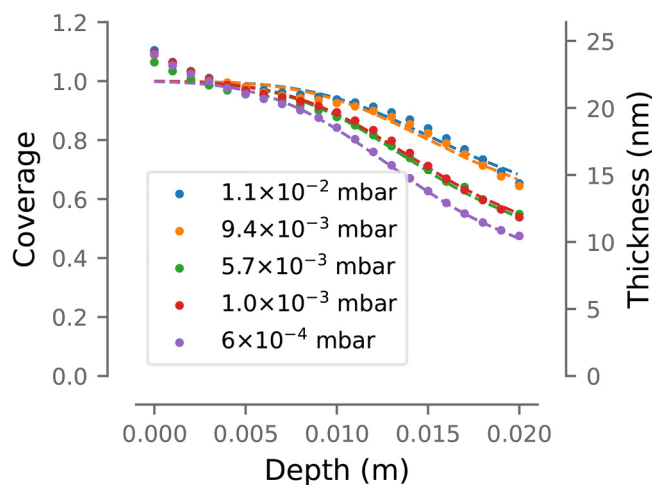


FIG. 12. Normalized deposition thickness profiles (dots) and simulated conformality profiles (lines) for depositions where the pressure was varied for a fixed power of 150 W and a pulse time of 5 s.

realize that the effect of the recombination coefficient manifests itself most clearly in the recombination-limited regime,²⁶ while variations in exposure will be most visible in the reaction- and diffusion-limited regime. The conditions we used are deliberately chosen to be in the diffusion-limited regime. By fixing the recombination coefficient, the error on all other parameters decreases an order of magnitude, precisely because these data are less suited to determine this coefficient.

While the fits are not perfect, from the agreement in slope between data and the profiles, we conclude that the obtained sticking coefficient of 0.316 ± 0.004 (for the power-varied profiles) and 0.172 ± 0.003 (for the pressure-varied profiles) is modeled correctly. These values had to be treated differently because the deposition temperature was different (100°C for the power-varied profiles and 120°C for the pressure-varied profiles). Other factors affecting the sticking may be the fact that the pressure-varied profiles are nearly saturated and that we adopt immediate thermalization of the gas in the simulation. That is, the gas temperature inside the HAR structure equals the wall temperature. To the best of our knowledge, there are no literature values for the sticking coefficient of oxygen radicals in the TMA- O_2^+ process. The obtained probabilities are high [compared to, for example, the TMA- H_2O process where the sticking coefficient of TMA is $(0.8-2) \times 10^{-3}$ and that of water $(0.5-2) \times 10^{-4}$].⁵¹ This is to be expected for a plasma-enhanced process, given the quick saturation times. Some imperfect Langmuir behavior is visible at the entrance: the thickness is a bit larger than the expected 22 nm with a small decrease over the first measurement points. This is as well the case in other reports.²⁶

The fitted exposures can be rescaled to reflect the partial pressure of oxygen radicals. To this aim, the exposures were divided by the pulse times, and the number of surface sites was taken into account via $s_0 = 1 \times 10^{-18} \text{ m}^2$, the area per surface site and, tentatively, a mass of 16 (the mass of atomic O), and a substrate temperature of $T = 393.15 \text{ K}$.

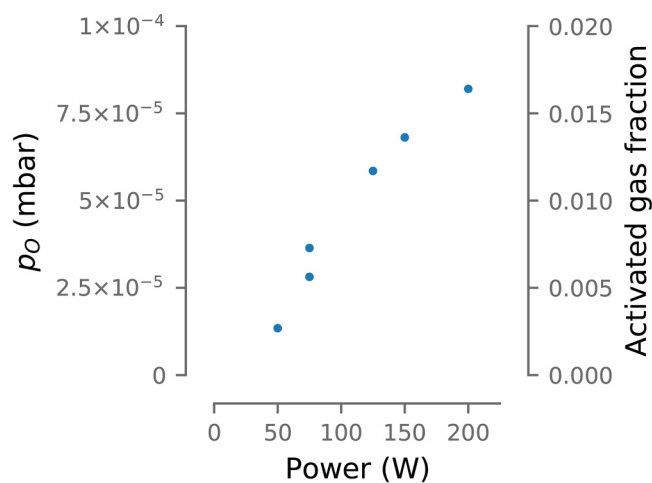


FIG. 13. Partial pressure of active species at different plasma powers for a fixed pressure of $5 \times 10^{-3} \text{ mbar}$ as measured by fitting conformality profiles to deposition thickness profiles. An attempt was made to draw error bars based on the fitting error but they were too small to be visible (order of magnitude $< 1\%$).

It can be readily seen that a higher power results in a higher partial pressure of the active species, and that this behavior is, again, linear with power (Fig. 13). The fact that the partial pressures of the two depositions at 75 W are so close to each other is as well reassuring. An increase in flow/pressure seems to increase the partial pressure of reactive species only moderately (Fig. 14). The rescaling and unit conversion are useful to convert the simulation output to experimentally meaningful values, but it should be noted that additional errors might be introduced here. The error bars shown in Figs. 13 and 14 only reflect the fit error and are too small to be visible. The linear trend is also visible when the simulation output is directly divided by the pulse time: errors in the rescaling only affect the slope of the line.

While from this experiment it cannot be concluded what the active species are (it could be O as well as metastable excited O_2 , see Fig. 5), the knowledge that higher power causes a linear increase in the partial pressure of the active species responsible for ALD surface reactions is very useful. Increasing the power might offer a way to coat high-aspect ratio structures in the recombination-limited regime still in reasonable times.

E. Limitations

It is important to define the limits of our approach as well. Optical spectra show only the radiative transitions of excited species in a particular wavelength range, leading to insensitivity to the negative ions. The concentration of metastable $^1\Delta_g$ molecular oxygen could not be estimated due to the self-absorption of these peaks in the IR. Relying on optical measurements too much means as well that we are blind toward nonradiative processes. Furthermore, the excitation rate coefficients may greatly differ between species, leading to a skewed perception of the composition of the gas if a naive integration is performed.

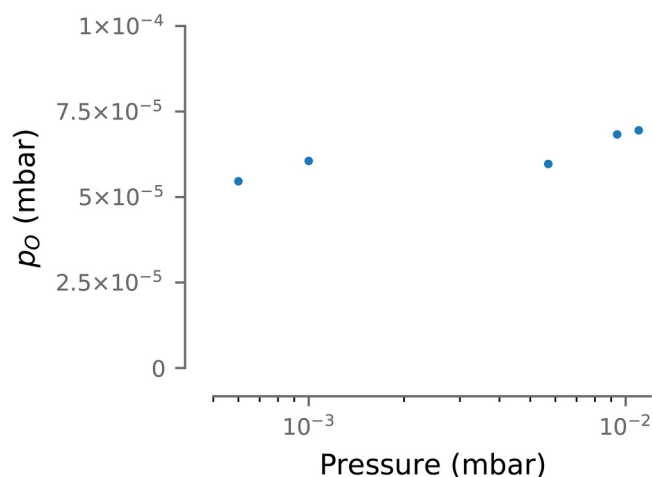


FIG. 14. Partial pressure of active species at different gas pressures for a fixed power of 150 W, as measured by fitting conformity profiles to deposition thickness profiles. An attempt was made to draw error bars based on the fitting error but they were too small to be visible (order of magnitude $<1\%$).

Optical spectra might as well be collected in the remote region. However, the benefits of plasma characterization are limited. The plasma is typically transparent in this region, and photons reflected off walls coming from the core of the plasma may reach the detector as easily as photons created in the remote region. This makes it hard to compare measurements across reactors. Also, the discrepancy between the number of ground state species and excited species may be exaggerated in the remote region. Because of the lack of exciting electrons in this region, the concentration of species with a low de-excitation rate coefficient will be overestimated: these may live longer and emit a photon downstream. Because of this, we lose sensitivity toward species with short-lived excited states, while they still might be present.

EQP results depend on the calibration of the detector. The transmission factor of the device depends on the nature and energy of the ions. Because peak positions for compared spectra were at similar energies, we assume this did not make a large impact on our measurements. Energy spectra are proportional to the fluxes but the calibration factor might be different for different species.

In this work, a wide parameter space was investigated but the obtained results should not be generalized beyond this parameter space. One phenomenon that should be highlighted is the effect of nonradiative recombination or decay. This can be seen from the discrepancy in ion concentrations if we compare O_2^+ trends for OES and EQP measurements, respectively, in the plasma and remote regions. At higher pressures, nonradiative processes may become more prevalent, potentially further confining the plasma and introducing unexpected effects.

As opposed to the automated OES and EQP measurements, conformity experiments and analyses are rather time consuming; hence, the relatively limited parameter space is probed in this section. While the fit error is very small and the simulated deposition profile agrees well with the experimental data, additional

errors might be introduced upon rescaling exposures to partial pressures. The observed trends (linear increase with power, little effect of pressure) will, however, remain valid.

The importance of reactor design and gas flow is shown by the results on bubble formation. While we see a clear effect from the pressure, we can for now only speculate on the reason why the change in gas inlet position causes this effect. Also, others have reported on such reactor-dependent effects.^{19,54} A final consideration can be made on the effect of plasma geometries and frequencies on plasma properties. The former will influence the species reaching the substrate due to recombination at walls and the direction of field lines, while the latter will influence plasma temperatures and collision processes. Hence, proper reactor design and choice of a plasma source fit for the goal of the deposition may be important as well.

IV. CONCLUSIONS AND OUTLOOK

One of the main limitations of PEALD is the conformality, which is often poor compared to thermal ALD. In the diffusion-limited regime, complex features become harder to coat with $\Psi_{\text{full coating}} \propto AR^2$ with AR the aspect ratio. On the other hand, if the active species recombine, as is the case for PEALD processes, the deposition quickly bogs down in the recombination-limited regime: the majority of the reactive species recombine at the entrance of the structure, and $\Psi_{\text{full coating}} \propto \exp(AR)$. To reduce the time necessary to fully cover the structure and to optimize process conditions, it is important to maximize the density of reactive species near the entrance of the HAR structure.

The findings of this work are summarized in a schematic way in Fig. 15. Our measurements suggest that optimal deposition conditions can be achieved by using the maximal attainable gas throughput (flow) and maximal plasma power. A high plasma power increases the electron density and radical partial pressure. It also increases the atom-to-ion ratio (which is beneficial if we can

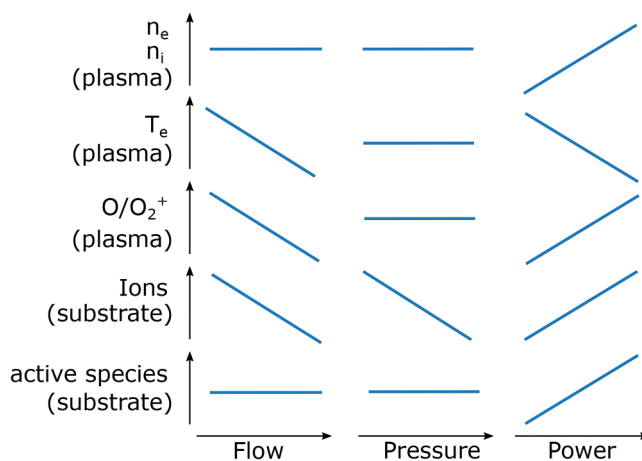


FIG. 15. Schematic summary of the findings in this work for an RF inductively coupled O_2 plasma.

consider the oxygen atoms responsible for the growth). A high gas throughput seems to increase the atom-to-ion ratio as well in OES measurements. However, the effect of an increased flow (or pressure) on growth processes is rather limited. It seems that the true benefit of working at high flows and pressures is the increase of loss processes for ions, decreasing the number of ions reaching the surface. As an added benefit, increasing the flow might help in preventing redeposition from reaction products.⁵⁵

The data collected in this work contribute only a small part to the broad range of possible experiments that can be conducted around this topic. Of course also, other plasmas are to be examined: we expect diatomic plasmas (H_2 , N_2) to behave in a similar way, although the complexity of N radicals might obscure the results and there are side-reactions possible of N_2 with the SiO_2 of the glass column. Characterizing NH_3 , H_2S , H_2O , and mixed plasmas would be even more challenging, as they consist of multiple intertwined components. Basic insights can be gathered by obtaining OES and mass spectrometry data, combined with conformality profile analysis.

ACKNOWLEDGMENTS

The authors acknowledge financial support from the UGENT-GOA-01G01019 project. Andreas Werbrouck acknowledges the Fund for Scientific Research—Flanders (FWO) for a scholarship through an SB Grant (No. 1S12319N). The authors thank Stefaan Broekaert and Jo Sys for their outstanding technical support, and for this work, in particular, in adapting the EQP vacuum chamber. Claire Greenwood from Hiden Analytical is acknowledged for her technical help with the EQP. Olivier Janssens is acknowledged for his SEM expertise and assistance with those measurements. Reinert Verstraete is acknowledged for some literature suggestions, Wouter Leroy for a discussion and suggestions on EQP calibration, David van der Heggen for discussions on spectrophotometer calibrations, and, finally, Véronique Cremers for discussions on conformality.

DATA AVAILABILITY

The data that support the findings of this study are available from the corresponding author upon reasonable request.

REFERENCES

- ¹V. Miiikkulainen, M. Leskelä, M. Ritala, and R. L. Puurunen, *J. Appl. Phys.* **113**, 021301 (2013).
- ²H. C. M. Knoop, T. Faraz, K. Arts, and W. M. M. E. Kessels, *J. Vac. Sci. Technol. A* **37**, 030902 (2019).
- ³M. A. Lieberman and A. J. Lichtenberg, *Principles of Plasma Discharges and Materials Processing* (Wiley, New York, 2005).
- ⁴G. Carter, *J. Phys. D: Appl. Phys.* **27**, 1046 (1994).
- ⁵H. B. Profijt, P. Kudlacek, M. C. M. van de Sanden, and W. M. M. Kessels, *J. Electrochem. Soc.* **158**, G88 (2011).
- ⁶K. Arts, J. H. Deijkers, T. Faraz, R. L. Puurunen, W. M. M. E. Kessels, and H. C. M. Knoop, *Appl. Phys. Lett.* **117**, 031602 (2020).
- ⁷D. Hoffman and J. A. Thornton, *J. Vac. Sci. Technol.* **20**, 355 (1982).
- ⁸E. Chason, M. Karlson, J. Colin, D. Magnfält, K. Sarakinos, and G. Abadias, *J. Appl. Phys.* **119**, 145307 (2016).
- ⁹B. Vermang, H. Goverde, V. Simons, I. De Wolf, J. Meersschaut, S. Tanaka, J. John, J. Poortmans, and R. Mertens, "A study of blister formation in ALD

Al_2O_3 grown on silicon," in *2012 38th IEEE Photovoltaic Specialists Conference* (IEEE, New York, 2012), pp. 001135–001138.

- ¹⁰O. Beldarrain, M. Duch, M. Zabala, J. M. Rafi, M. B. González, and F. Campabadal, *J. Vac. Sci. Technol. A* **31**, 01A128 (2013).
- ¹¹M. Broas, H. Jiang, A. Graff, T. Sajavaara, V. Vuorinen, and M. Paulasto-Kröckel, *Appl. Phys. Lett.* **111**, 141606 (2017).
- ¹²H. Liu, S. Guo, R. B. Yang, C. J. Lee, and L. Zhang, *ACS Appl. Mater. Interfaces* **9**, 26201 (2017).
- ¹³A. S. Kuznetsov, M. A. Gleeson, and F. Bijkerk, *J. Appl. Phys.* **115**, 173510 (2014).
- ¹⁴O. M. Ylivaara *et al.*, *Thin Solid Films* **552**, 124 (2014).
- ¹⁵T. Lüdera, T. Lauermann, A. Zuschlag, G. Hahn, and B. Terheiden, *Energy Procedia* **27**, 426 (2012).
- ¹⁶R. Müller *et al.*, *Coatings* **8**, 413 (2018).
- ¹⁷P. Genevée, E. Ahiavi, N. Janunts, T. Pertsch, M. Oliva, E.-B. Kley, and A. Szeghalmi, *J. Vac. Sci. Technol. A* **34**, 01A113 (2016).
- ¹⁸H. Profijt, M. Van de Sanden, and W. Kessels, *J. Vac. Sci. Technol. A* **31**, 01A106 (2013).
- ¹⁹M. Napari, M. Lahtinen, A. Veselov, J. Julin, E. Østrenge, and T. Sajavaara, *Surf. Coat. Technol.* **326**, 281 (2017).
- ²⁰T. Faraz *et al.*, *ACS Appl. Mater. Interfaces* **10**, 13158 (2018).
- ²¹D. R. Boris, V. D. Wheeler, J. R. Avila, S. B. Qadri, C. R. Eddy, and S. G. Walton, *J. Vac. Sci. Technol. A* **37**, 060909 (2019).
- ²²V. D. Wheeler *et al.*, *Chem. Mater.* **32**, 1140 (2020).
- ²³H.-Y. Shih, W.-H. Lee, W.-C. Kao, Y.-C. Chuang, R.-M. Lin, H.-C. Lin, M. Shiojiri, and M.-J. Chen, *Sci. Rep.* **7**, 1 (2017).
- ²⁴J. Dendooven, D. Deduytsche, J. Musschoot, R. L. Vanmeirhaeghe, and C. Detavernier, *J. Electrochem. Soc.* **157**, G111 (2010).
- ²⁵H. C. M. Knoop, E. Langereis, M. C. M. van de Sanden, and W. M. M. Kessels, *J. Electrochem. Soc.* **157**, G241 (2010).
- ²⁶K. Arts, M. Utriainen, R. L. Puurunen, W. M. M. Kessels, and H. C. M. Knoop, *J. Phys. Chem. C* **123**, 27030 (2019).
- ²⁷V. Cremers, R. L. Puurunen, and J. Dendooven, *Appl. Phys. Rev.* **6**, 021302 (2019).
- ²⁸See the supplementary material at <https://www.scitation.org/doi/suppl/10.1116/6.0001094> for more information on the probed parameter space, the operating principle of an inductively coupled plasma source compared to that of a capacitively coupled source, UV/VIS spectra of the plasma with varying pressure at constant power, additional plots of the data in Fig. 6, a comparison of our code with the Machball package (Ref. 33).
- ²⁹D. R. Boris, V. D. Wheeler, N. Nepal, S. B. Qadri, S. G. Walton, and C. C. R. Eddy, *J. Vac. Sci. Technol. A* **38**, 040801 (2020).
- ³⁰S. Tinck and A. Bogaerts, *Plasma Sources Sci. Technol.* **20**, 015008 (2011).
- ³¹P. Lei, W. Leroy, B. Dai, J. Zhu, X. Chen, J. Han, and D. Depla, *Surf. Coat. Technol.* **276**, 39 (2015).
- ³²C. Muratore, J. J. Moore, and J. A. Rees, *Surf. Coat. Technol.* **163–164**, 12 (2003).
- ³³V. Cremers, F. Geenen, C. Detavernier, and J. Dendooven, *J. Vac. Sci. Technol. A* **35**, 01B115 (2017).
- ³⁴A. Yanguas-Gil and J. W. Elam, *Theor. Chem. Acc.* **133**, 72 (2014).
- ³⁵T. S. Cale, G. B. Raupp, and T. H. Gandy, *J. Appl. Phys.* **68**, 3645 (1990).
- ³⁶A. J. M. Mackus, S. B. S. Heil, E. Langereis, H. C. M. Knoop, M. C. M. van de Sanden, and W. M. M. Kessels, *J. Vac. Sci. Technol. A* **28**, 77 (2010).
- ³⁷H. Jung *et al.*, *ACS Appl. Mater. Interfaces* **10**, 40286 (2018).
- ³⁸S. J. Northway and R. C. Fry, *Appl. Spectrosc.* **34**, 332 (1980).
- ³⁹S. Bashkin and J. O. Stoner, *Atomic Energy Levels and Grotrian Diagrams: Hydrogen I-Phosphorus XV* (Elsevier, New York, 2013).
- ⁴⁰P. H. Krupenie, *J. Phys. Chem. Ref. Data* **1**, 423 (1972).
- ⁴¹R. W. B. Pearse and A. G. Gaydon, *Identification of Molecular Spectra* (Chapman and Hall, London, 1976).
- ⁴²R. M. Badger, A. C. Wright, and R. F. Whitlock, *J. Chem. Phys.* **43**, 4345 (1965).
- ⁴³U. Fantz, *Plasma Sources Sci. Technol.* **15**, S137 (2006).

- ⁴⁴A. Annušová, D. Marinov, J.-P. Booth, N. Sirse, M. L. da Silva, B. Lopez, and V. Guerra, *Plasma Sources Sci. Technol.* **27**, 045006 (2018).
- ⁴⁵M. Napari, O. Tarvainen, S. Kinnunen, K. Arstila, J. Julin, Ø. S. Fjellvåg, K. Weibye, O. Nilsen, and T. Sajavaara, *J. Phys. D: Appl. Phys.* **50**, 095201 (2017).
- ⁴⁶J. T. Gudmundsson and E. G. Thorsteinsson, *Plasma Sources Sci. Technol.* **16**, 399 (2007).
- ⁴⁷R. Gordon, D. Hausmann, E. Kim, and J. Shepard, *Chem. Vap. Deposition* **9**, 73 (2003).
- ⁴⁸A. Yanguas-Gil and J. W. Elam, *Chem. Vap. Deposition* **18**, 46 (2012).
- ⁴⁹M. Ylilammi, O. M. E. Ylivaara, and R. L. Puurunen, *J. Appl. Phys.* **123**, 205301 (2018).
- ⁵⁰J. Dendooven, D. Deduytsche, J. Musschoot, R. L. Vanmeirhaeghe, and C. Detavernier, *J. Electrochem. Soc.* **156**, P63 (2009).
- ⁵¹K. Arts, V. Vandalon, R. L. Puurunen, M. Utriainen, F. Gao, W. M. M. E. Kessels, and H. C. M. Knoop, *J. Vac. Sci. Technol. A* **37**, 030908 (2019).
- ⁵²J. Yim, O. M. Ylivaara, M. Ylilammi, V. Korpelainen, E. Haimi, E. Verkama, M. Utriainen, and R. L. Puurunen, *Phys. Chem. Chem. Phys.* **22**, 23107 (2020).
- ⁵³J. Greaves and J. Linnett, *Trans. Faraday Soc.* **55**, 1346 (1959).
- ⁵⁴M. J. Sowa, *J. Vac. Sci. Technol. A* **32**, 01A106 (2014).
- ⁵⁵H. C. M. Knoop, K. de Peuter, and W. M. M. Kessels, *Appl. Phys. Lett.* **107**, 014102 (2015).